Impact of Gravitational Lensing on Cosmology
Proceedings IAU Symposium No. 225, 2004
Mellier, Y. & Meylan,G. eds.

doi:10.1017/S174392130500205X

Galaxy-Galaxy Lensing Studies from COMBO-17

Martina Kleinheinrich[1], Hans-Walter Rix[1], Peter Schneider[2], Thomas Erben[2], Klaus Meisenheimer[1], Christian Wolf [3], and Mischa Schirmer[4]

[1]Max-Planck-Institut für Astronomie, Königstuhl 17, D-69117 Heidelberg, Germany

[2]Institut für Astrophysik und Extraterrestrische Forschung, Universität Bonn, Auf dem Hügel 71, D-53121 Bonn, Germany

[3]Department of Physics, Denys Wilkinson Bldg., University of Oxford, Keble Road, Oxford, OX1 3RH, U.K.

[4]Isaac Newton Group of Telescopes, Apartado de correos 321, E-38700 Santa Cruz de La Palma, Spain

Abstract. We study the dark matter halos of galaxies with galaxy-galaxy lensing using the COMBO-17 survey. This survey offers an unprecedented data set for studying lens galaxies at $z = 0.2 - 0.7$ including redshift information and spectral classification from 17 optical filters for objects brighter than $R = 24$. So far, redshifts and classification for the lens galaxies have mainly been available for local surveys like the Sloan Digital Sky Survey (SDSS). Further, redshifts for the source galaxies have typically not been available at all but had to be estimated from redshift probability distribution which – for faint surveys – even had to be extrapolated.

To study the dark matter halos we parametrize the lens galaxies as singular isothermal spheres (SIS) or by Navarro-Frenk-White (NFW) profiles. In both cases we find a dependence of the velocity dispersion or virial radius, respectively, on lens luminosity and colour. For the SIS model, we are able to reproduce the Tully-Fisher/Faber-Jackson relation on a scale of $150h^{-1}$ kpc. For the NFW profile we also calculate virial masses, mass-to-light ratios and rotation velocities.

Finally, we investigate differences between the three survey fields used here.

1. Outline of the method

Galaxy-galaxy lensing uses the distortions of background galaxies to study the mass distribution around foreground galaxies. In a typical lens situation, the shear from a foreground lens is only weak. Therefore, galaxy-galaxy lensing can only study dark matter halos of galaxies statistically by averaging over thousands of lens galaxies. For reviews on galaxy-galaxy lensing see Mellier (1999) and Bartelmann & Schneider (2001).

We use the maximum-likelihood technique proposed by Schneider & Rix (1997). First, we have to identify lenses and source galaxies which we do based on accurate photometric redshifts. Next, we adopt a specific lens model to calculate for each background galaxy the shear contributions from each foreground galaxy within a certain annulus. The estimated shear is compared to the observed shapes of the sources for a range of input parameters of the lens model and those parameters which maximize the likelihood are determined. Here, we use the singular isothermal sphere (SIS) and the Navarro-Frenk-White (NFW) profile to model the lenses.

We adopt $(\Omega_m, \Omega_\Lambda) = (0.3, 0.7)$ and $H_0 = 100h$ km s^{-1}Mpc^{-1}.

2. Data: The COMBO-17 survey

For our investigation we use the COMBO-17 survey (Wolf *et al.* (2004)) which is a deep survey with very good imaging quality and accurate photometric redshifts. All data are taken with the Wide Field Imager at the MPG/ESO 2.2-m telescope on La Silla, Chile. The survey consists of 4 fields of which 3 are used here. The limiting magnitude is $R \approx 25.5$. Deep R-band observations were taken in the best seeing conditions (below 0.8" PSF). Observations in $UBVRI$ and 12 medium-band filters are used to derive restframe colours and accurate photometric redshifts with $\sigma_z < 0.1$ at $R < 24$ and $\sigma_z < 0.01$ at $R < 21$. These allow us to select both lenses and sources based on their redshifts and to select and study subsamples of lens galaxies based on their restframe colours.

3. Results

In the following, sources are all galaxies with $R = 18-24$ and $z_{\rm s} = 0.3-1.4$. Lenses are galaxies with $R = 18-24$, $z_{\rm d} = 0.2-0.7$. The shear of a specific lens galaxy on a specific source galaxy is only considered if $z_{\rm d} < z_{\rm s} - 0.1$ for that lens-source pair. Further, the projected separation between lens and source must be smaller than $r_{\rm max} = 150h^{-1}$ kpc at the redshift of the lens when the lens is modelled as SIS. At this $r_{\rm max}$ we obtain the tightest constraints. When modelling lenses by NFW profiles we extend the maximum separation to $r_{\rm max} = 400h^{-1}$ kpc to ensure that the region around the virial radius is probed. Due to the size of galaxy images, a minimum angular separation of 8" between lenses and sources is required in order to avoid that shape measurements of sources are biased by the light of the lenses.

We investigate the lens sample as a whole and additionally split it into red and blue subsamples based on restframe colours. Galaxies with $< U - V > \leqslant 1.15 - 0.31 \times z - 0.08(M_V - 5\ log\ h + 20)$ define the blue sample while all other galaxies are in the red sample (Bell *et al.* (2004)).

3.1. *SIS and Tully-Fisher/Faber-Jackson relation*

The density profile of the SIS is given by $\rho(r) = \sigma_{\rm v}^2/2\pi G r^2$ where $\sigma_{\rm v}$ is the velocity dispersion and r is the distance from the center of the lens. We assume that the velocity dispersion depends on the luminosity of a galaxy, $\sigma_{\rm v}/\sigma_\star = (L/L_\star)^\eta$, where $L_\star = 10^{10}h^{-2}L_\odot$ is a characteristic luminosity measured in the restframe SDSS r-band. This is the Tully-Fisher or Faber-Jackson relation which was derived for galaxies on smaller scales than used here from their rotation curves or stellar velocity dispersion.

The left panel of Figure 1 shows 1-, 2- and 3-σ contours for the model parameters $\sigma_\star$ and η derived for the whole lens sample. The best-fit parameters with 1-σ errors are $\sigma_\star = 156^{+18}_{-18}$ km/s and $\eta = 0.28^{+0.12}_{-0.09}$. These values agree very well with expectations from e.g. rotation curve measurements.

We want to compare this result to the galaxy-galaxy lensing measurement from the Red-Sequence Cluster Survey (RCS, Hoekstra, Yee & Gladders (2004)) which probes lens galaxies in a comparable redshift range and uses a similar modelling. Hoekstra, Yee & Gladders (2004) find $\sigma_\star = 140 \pm 4$ km/s at fixed $\eta = 0.3$. However, Hoekstra, Yee & Gladders (2004) use a characteristic luminosity of $L_B = 10^{10}h^{-2}L_\odot$ measured in the B-band instead of the r-band as we do here. From the restframe luminosities of galaxies in COMBO-17 we estimate that galaxies with $L_B = 10^{10}h^{-2}L_\odot$ have $L_r = 1.25 \times 10^{10}h^{-2}L_\odot$. Further, Hoekstra, Yee & Gladders (2004) use pairs with projected separations up to 2' corresponding to about $r_{\rm max} = 350h^{-1}$ kpc. Although for the SIS model the velocity dispersion should be independent of radius, we find a decline of the fitted $\sigma_\star$ with increasing $r_{\rm max}$. Using $L_\star = 1.25 \times 10^{10}h^{-2}L_\odot$ and $r_{\rm max} = 350h^{-1}$ kpc

https://doi.org/10.1017/S174392130500205X Published online by Cambridge University Press

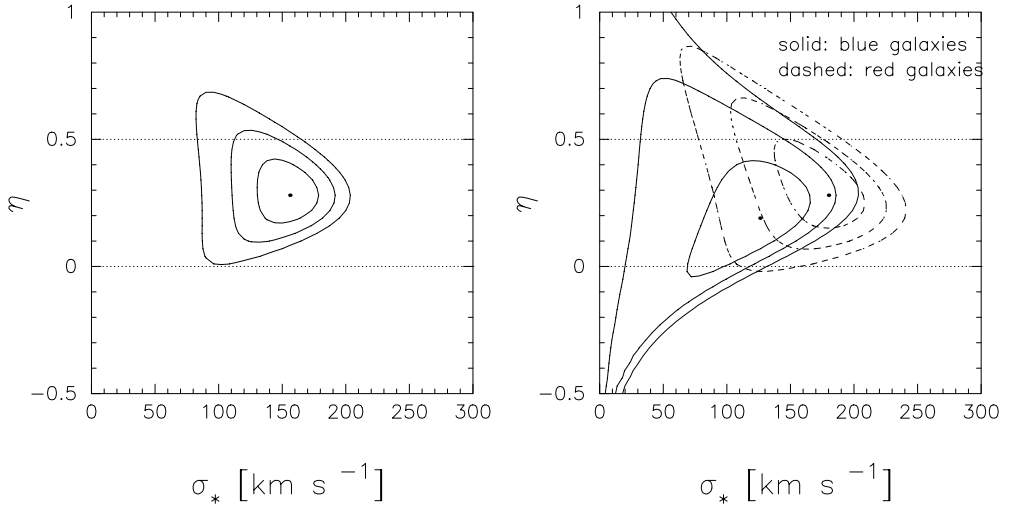

Figure 1. Constraints on dark matter halos modelled as SIS. The left panel uses the whole lens sample. In the right panel, the lens sample is split into blue and red lenses.

we measure $\sigma_\star = 138^{+18}_{-24}$ km/s and $\eta = 0.34^{+0.18}_{-0.12}$ in very good agreement with the RCS result.

The error on $\sigma_\star$ is about 5 times smaller for the RCS than for COMBO-17. Given the about 60 times larger area of the RCS this is not surprising. The uncertainties should also be influenced by the qualitiy of the redshift information. The measurement from the RCS uses observations in a single passband only and does therefore not have redshift estimates for individual objects. In Kleinheinrich *et al.* (2004) we find that the velocity dispersion can be well constrained even in the absence of redshift information. Redshifts for individual lens galaxies reduce the errors on $\sigma_\star$ by only 15%. However, they are essential for measuring the dependence of the velocity dispersion (or mass) on luminosity – the errors on η increase by a factor of 2.5 when omitting the lens redshifts. Individual redshifts for the sources are not important as long as the redshift distribution is known.

The right panel of Figure 1 shows likelihood contours for the blue and red subsamples. While no significant change in η is seen, a 2-σ difference in $\sigma_\star$ is seen between the two lens populations. The best-fit velocity dispersions are $\sigma_\star = 126^{+30}_{-36}$ km/s for the blue sample and $\sigma_\star = 180^{+24}_{-30}$ km/s for the red sample, respectively. The red sample consists of 2579 galaxies, the blue sample of 9898 galaxies. Although only about 20% of the lenses are red, this subsample gives even tighter constraints than the blue subsample. This shows clearly that most of the galaxy-galaxy lensing signal comes from red galaxies.

3.2. *NFW and 'Tully-Fisher/Faber-Jackson' relation*

Next, we model lens galaxies by NFW profiles. The density profile is given by $\rho(r) = \delta_c/(r/r_s(1+r/r_s)^2)$. r_s is a characteristic scale radius at which the density profile changes from $\rho(r) \propto r^{-1}$ to $\rho(r) \propto r^{-3}$. δ_c is related to the concentration c. The virial radius $r_{\rm vir}$ is defined by $r_{\rm vir} = r_s c$. Here, the virial radius is the radius inside which the mean density is 200 times the mean density of the Universe. The relation between δ_c and c is fixed by this definition. Unfortunately, the definition of the virial radius is not unique. Often, the critical density of the Universe instead of its mean density is referred to or overdensities different from 200 are used. These differences have to be kept in mind when comparing results from the NFW profile.

https://doi.org/10.1017/S174392130500205X Published online by Cambridge University Press

Motivated by the Tully-Fisher and Faber-Jackson relations we assume a relation between the virial radius and luminosity according to $r_{\rm vir}/r_{\rm vir,*} = (L/L_\star)^\eta$. As for the SIS, we adopt $L_\star = 10^{10}h^{-2}L_\odot$.

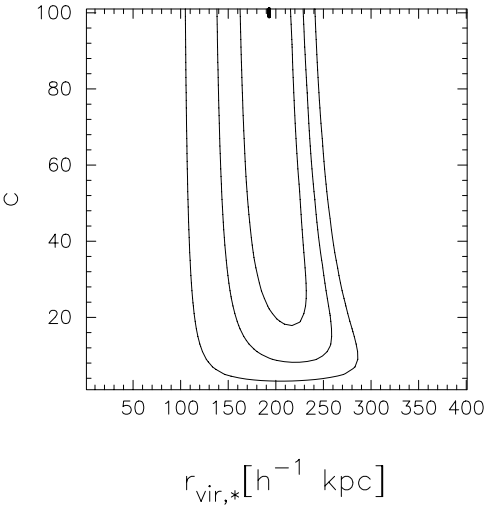

Figure 2. Constraints on dark matter halos modelled by NFW profiles, fitting virial radius $r_{\rm vir,\star}$ and concentration c.

First, we try to measure the virial radius $r_{\rm vir,*}$ and the concentration c at fixed $\eta = 0.3$, see Fig. 2. The virial radius can be constrained well while on the concentration we can only derive lower limits. This implies an upper limit on the scale radius, $r_s < 10h^{-1}$ kpc. This is at all considered lens redshifts smaller than the imposed minimum angular separation between lenses and sources of 8". Therefore, we cannot expect to be sensitive to r_s or c. In the following, we fix $c = 20$ which is at the lower end of the values allowed by our measurement. Note that when defining the virial radius as radius inside which the mean density is 200 times the critical density of the Universe (instead of its mean density as done here) this would refer to $c = 12.5$. Correspondingly, the virial radii and virial masses which we are going to derive would be smaller in that case by about 40% and 20%, respectively.

Figure 3 shows 1-, 2- and 3-σ contours for the virial radius $r_{\rm vir,*}$ and η for the whole lens sample and for the blue and red subsamples. Averaged over all lenses, the best-fit parameters with 1-σ errors are $r_{\rm vir,*} = 217^{+24}_{-32}h^{-1}$ kpc and $\eta = 0.30^{+0.16}_{-0.12}$. For the blue sample we find $r_{\rm vir,*} = 177^{+40}_{-56}h^{-1}$ kpc and $\eta = 0.18^{+0.16}_{-0.16}$, for the red sample $r_{\rm vir,*} = 233^{+48}_{-48}h^{-1}$ kpc and $\eta = 0.38^{+0.16}_{-0.20}$. Between the blue and red subsamples we measure a 1-σ difference in the virial radius as well as in η.

Table 3.2 gives an overview of the measured parameters ($r_{\rm vir,*}$, η) and calculated quantities like the virial mass $M_{\rm vir,*}$, virial mass-to-light ratio $M_{\rm vir,*}/L$ and the scaling between $M_{\rm vir,*}/L$ and luminosity.

Again, we compare our results to those from other data sets. Hoekstra, Yee & Gladders (2004) find from the RCS $M_{\rm vir,*} = 8.4 \pm 0.7 \times 10^{11}h^{-1}M_\odot$ at $L_B = 10^{10}h^{-2}L_\odot$. At the corresponding $L_\star = 1.25 \times 10^{10}h^{-2}L_\odot$ measured in the restframe r-band we find $M_{\rm vir,*} = 8.0^{+3.9}_{-3.0} \times 10^{11}h^{-1}M_\odot$. Guzik & Seljak (2002) obtain $M_{\rm vir,*} = 8.96 \pm 1.59 \times 10^{11}h^{-1}M_\odot$ at $L_\star = 1.51 \times 10^{10}h^{-2}L\odot$ from the SDSS where $L_\star$ is measured in the SDSS restframe r-band. However, Guzik & Seljak (2002) define the virial radius as radius inside which the mean density is 200 times the critical density of the Universe. Our

https://doi.org/10.1017/S174392130500205X Published online by Cambridge University Press

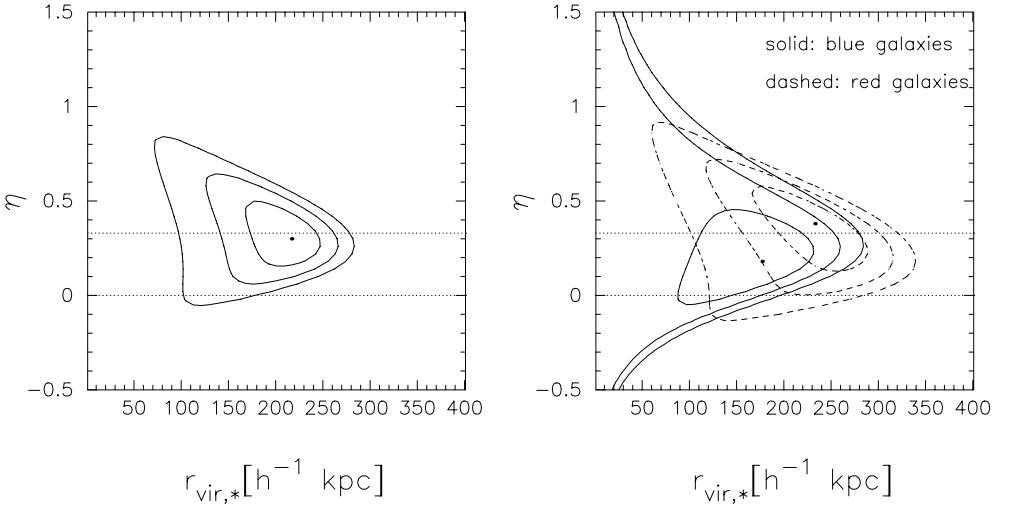

Figure 3. Constraints on dark matter halos modelled by NFW profiles, fitting virial radius $r_{\rm vir,\star}$ and its dependence on luminosity (η). The left panel uses the whole lens sample. In the right panel, the lens sample is split into blue and red lenses.

Table 1. Constraints on dark matter halos of galaxies modelled by NFW profiles. The virial radius $r_{\rm vir,*}$ and η are fitted quantities (see Fig. 3), the virial mass $M_{\rm vir,*}$, the virial mass-to-light ratio $M_{\rm vir,*}/L$ and the rotation velocity at the virial radius, $v_{\rm vir,*}$, are calculated from $r_{\rm vir,*}$. $\beta = 3\eta - 1$ gives the scaling of $M_{\rm vir,*}/L$ with luminosity, $M_{\rm vir,*}/L \propto L^{\beta}$. The maximum rotation velocity $v_{\rm max}$ and the radius of the maximum rotation velocity $r(v_{\rm max})$ are calculated for a concentration $c = 20$.

	$r_{\rm vir,*}$ $[h^{-1}$ kpc$]$	η	$M_{\rm vir,*}$ $[10^{11}h^{-1}M_\odot]$	$M_{\rm vir,*}/L$ $[h(M/L)_\odot]$	β	$v_{\rm vir,*}$ [km/s]	$v_{\rm max}$ [km/s]	$r(v_{\rm max})$ $[h^{-1}$ kpc$]$
all	217^{+24}_{-32}	$0.30^{+0.16}_{-0.12}$	$7.1^{+2.6}_{-2.7}$	71^{+26}_{-27}	$-0.10^{+0.48}_{-0.36}$	119^{+13}_{-18}	169^{+19}_{-25}	$23.4^{+2.6}_{-3.4}$
blue	177^{+40}_{-56}	$0.18^{+0.16}_{-0.16}$	$3.9^{+3.3}_{-2.6}$	39^{+33}_{-26}	$-0.46^{+0.48}_{-0.48}$	97^{+22}_{-31}	138^{+33}_{-44}	$19.1^{+4.3}_{-6.0}$
red	233^{+48}_{-48}	$0.38^{+0.16}_{-0.20}$	$8.8^{+6.7}_{-4.4}$	88^{+67}_{-44}	$0.14^{+0.62}_{-0.60}$	128^{+26}_{-26}	181^{+38}_{-36}	$25.2^{+5.1}_{-5.2}$

corresponding result using their value of $L_\star$ and their definition of the virial radius is $M_{\rm vir,*} = 7.8^{+3.5}_{-2.7} \times 10^{11}h^{-1}M_\odot$.

3.3. *Individual fields*

Finally, we investigate the three survey fields used here individually and address the question whether they give consistent results. Figure 4 shows likelihood contours from fitting the SIS model as in Sect. 3.1. Clearly, the derived constraints on the velocity dispersion $\sigma_\star$ are not consistent for the individual fields. While the A901 field gives very tight constraints, from the CDFS we can only derive an upper limit on $\sigma_\star$. The deviation from the measurement that uses all three fields together ($\sigma_\star = 156$ km/s) is 1-σ towards higher values for the A901 field and 2-σ towards lower values for the CDFS field. Only the S11 field is consistent with the overall measurement.

These three survey fields were already selected to be very different. The S11 field is the only random field. It contains the cluster Abell 1364 at $z = 0.11$ by chance. The A901 field was chosen because it contains a supercluster with the three components Abell 901a, 901b and 902 at $z = 0.16$. The CDFS field contains the Chandra Deep Field South and was chosen because of its emptiness. Due to these selection criteria one might suspect that the measured galaxy-galaxy lensing signal is mostly due the foreground clusters.

https://doi.org/10.1017/S174392130500205X Published online by Cambridge University Press

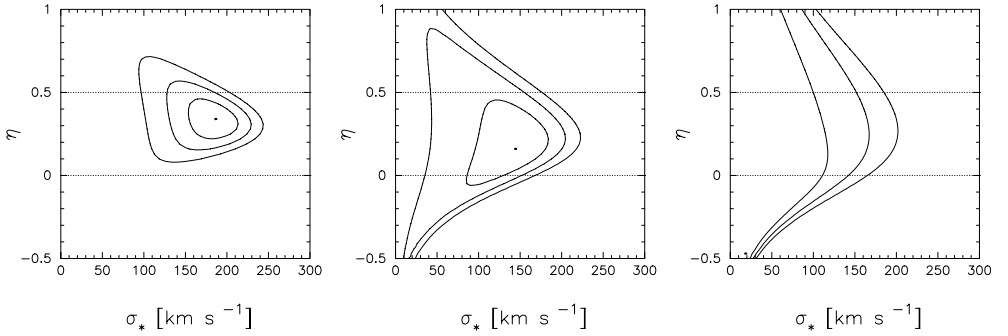

Figure 4. Constraints on dark matter halos modelled as SIS from the three individual survey fields. The left panel refers to the A901 field, the middle panel to the S11 field and the right panel to the CDFS field.

However, our lens sample only uses galaxies at $z > 0.2$ and should thus not include cluster galaxies. Therefore, the foreground clusters in the A901 and S11 field should not have any influence on our measurement. By including the additional shear from the foreground clusters we indeed confirm this assumption. Further, we find that the shear from an additional cluster in the A901 field at $z = 0.47$ does not induce a significant shift in the velocity dispersion. Including the shear from this higher-redshift cluster does however increase the uncertainties by about 20%.

Another suspected reason for the differences between the three fields is the imaging quality. The sum image of the A901 field has the best quality with a PSF of 0.74". The PSF of the other two sum images is 0.88". If image quality had a dominant effect, then the results from the S11 field and the CDFS field should be consistent. For the CDFS field we have several independent sum images available from different observing runs with very different seeing conditions and exposure times which yield consistent lensing signals. Therefore we rule out image quality as possible explanation for the discrepant measurements.

The most probable explanation we find for the deviating results comes from the number counts in the different fields. The number of lenses in the fields is 4636 (A901), 4268 (S11) and 3573 (CDFS). Therefore, one expects the tightest constraints from the A901 field. The difference in the derived velocity dispersion could be due to differences in the composition of the lens samples. Indeed, the fraction of red lenses is 23.5% in the A901 field, 20.5% in the S11 field and only 17.2% in the CDFS field. Given our findings in Sect. 3.1 we expect a higher velocity dispersion and tighter constraints with increasing fraction of red galaxies.

References

Bartelmann, M. & Schneider, P. 2001, *Physics Reports* 340, 291

Bell, E., Wolf, C., Meisenheimer, K., Rix, H.-W., Borch, A., Dye, S., Kleinheinrich, M., Wisotzki, L. & McIntosh, D.H. 2004, *A&A* 608, 752

Guzik, J. & Seljak, U. 2002, *MNRAS* 335, 311

Hoekstra, H., Yee, H.K.C. & Gladders, M. D. 2004, *ApJ* 606, 67

Kleinheinrich, M., Rix, H.-W., Erben, T., Schneider, P., Wolf, C., Schirmer, M., Meisenheimer, K., Borch, A., Dye, S., Kovacs, Z. & Wisotzki, L. 2004, *astro-ph/0404527*

Mellier, Y. 1999, *ARA&A* 37, 127

Schneider, P. and Rix, H.-W. 1997, *ApJ* 474, 25

Wolf, C., Meisenheimer, K., Kleinheinrich, M., Borch, A., Dye, S., Gray, M., Wisotzki, L., Bell, E., Rix, H.-W., Cimatti, A., Hasinger, G. & Szokoly, G. 2004, *A&A* 421, 913

https://doi.org/10.1017/S174392130500205X Published online by Cambridge University Press